Identification and Analysis of Recurringly Occluded Persistent Scatterers, with Application to Displacement Monitoring in the Oetztal Alps

Nils Dörr[1], Andreas Schenk[1]

[1] Institute of Photogrammetry and Remote Sensing, Karlsruhe Institute of Technology, Germany - (nils.doerr, andreas.schenk)@kit.edu

Keywords: Persistent Scatterer Interferometry, Time Series Analysis, Temporary Persistent Scatterers, Change Detection.

Abstract

The Persistent Scatterer Interferometry (PSI) is a powerful remote sensing technique for Earth surface displacement monitoring with potential sub-millimeter accuracy. It is based on identifying and analyzing point scatterers which provide coherent backscatter over time. Standard PSI approaches require these Persistent Scatterers (PSs) to be stable throughout the whole monitoring period. However, PSs can appear or disappear over time, due to construction work, natural decorrelation, or temporary occlusion by floods or snow. The integration of such Temporary PSs (TPSs) is needed to establish an optimum measurement point network. While a few TPS-integrating PSI algorithms have been proposed before, these were exclusively evaluated at construction sites. Here, we evaluate the capabilities of an existing algorithm to identify and analyze recurringly occluded PSs (ROPSs), which might be seasonally snow-covered or flooded. We show, based on simulated data, that a newly proposed CuSum algorithm outperforms the approach implemented in the tested algorithm at identifying the coherent time series segments of ROPSs. The displacement rate estimation becomes increasingly instable with increasing occlusion periods. Inadequately sampled seasonal movements can also lead to false displacement estimations, which must be identified and discarded. Finally, we present results from a Sentinel-1 experiment over the seasonally snow-covered Oetztal Alps. Integrating ROPSs significantly increases the measurement point density at many locations across the study area, compared to the European Ground Motion Service. While the algorithm did not identify coherent segments in each summer for most of the ROPS, their integration still leads to a significant information gain.

1. Introduction

1.1 Motivation

The Persistent Scatterer Interferometry (PSI) is a multi-temporal Interferometric Synthetic Aperture Radar (InSAR) technique, which enables to monitor displacements of the Earth's surface over time by examining the phase time series in SAR acquisition stacks (Ferretti et al., 2001; Hooper et al., 2007). The technique identifies and analyzes Persistent Scatterers (PSs), which are phase-stable scattering points that dominate the backscatter of the resolution cells they are located in, with potential sub-millimeter accuracy (Ferretti et al., 2007). One limitation of the technique is that standard PSI approaches only identify and analyze PSs that are visible and coherent throughout the entire analyzed SAR time series. However, PSs can fade, appear, or be occluded within the observation time series due to physical changes in the scene or changes in the acquisition geometry (Ferretti et al., 2003; Perissin and Ferretti, 2007). Such Temporary PSs (TPSs) should be integrated into PSI in order to establish optimal measurement point networks (Dörr et al., 2022b).

Dörr et al. (2022a) presented a method to fully integrate TPS into their PSI approach. They showed, based on a study of a Sentinel-1 data stack acquired over an urban area, that the overall measurement point density of their PSI algorithm was significantly increased by the TPS integration, and provided examples of appearing and fading TPS, whose coherence changes were triggered by construction work. However, the integration of other relevant TPS types into the PSI has not been evaluated yet. This includes TPSs with recurring occlusion periods. We refer to such pixels as recurringly occluded PSs (ROPSs), whose physical characteristics do not significantly change during incoherent periods, such as recurringly flooded pixels on reservoir bank slopes or seasonally snow-covered pixels, for example. The latter regularly occur in alpine regions, and are handled in operational PSI approaches, such as in the European Ground Motion Service (EGMS), by systematically excluding winter acquisitions from the PSI analysis. However, the set of excluded acquisitions cannot differ across whole scenes or bursts in the case of Sentinel-1, which means that usually too many scenes are excluded for lower-lying regions, which are affected by shorter snow-cover periods during winters than higher-lying regions. Therefore, it is desirable to automatically detect and exclude occlusion scenes on a per-pixel basis.

In this study, we evaluate the ability of the TPS integration algorithm by Dörr et al. (2022a) to robustly identify and analyze ROPSs. Furthermore, we compare the performance of individual algorithm components against alternative methods. The analyses are carried out on basis of simulated Synthetic Aperture Radar (SAR) stacks, as well as real Sentinel-1 data acquired over a high-alpine region in the Alps, which is affected by long periods of snow-cover during the year.

1.2 Related work

The occurrence and characteristics of TPSs have been first described in Ferretti et al. (2003). TPSs are scatterers which are only active in one or several sub-segments of the analyzed SAR time series. The basic idea for their incorporation into the PSI is to detect their coherent segments and analyze them with standard PSI approaches. Ferretti et al. (2003) observed that abrupt changes in the phase and coherence of a pixel correspond to abrupt changes in its amplitude. Based on that, they developed an Bayesian approach for detecting change points in amplitude time series between coherent and incoherent segments of TPSs assuming Gaussian statistics. Following their work, further amplitude-based change point detection algorithms were proposed that differ in the assumed statistics or the estimators (Ansari et al., 2014; Dogan and Perissin, 2014; Hu et al., 2019).

Dörr et al. (2022a) showed that while amplitude-based change point detection algorithms are fast and do not rely on error-prone phase processing steps, they do not always identify correct start and end times of TPSs. They showed an example of buildings constructions, where the amplitude-based start time estimation of TPSs was almost one year before the actual start of their coherent lifetime. The reason behind is that the pixels' backscatter amplitude increased during the construction phase, while phase-stability was only reached after the end of construction. This is why they proposed a secondary phase-based change point detection algorithm to refine the initial amplitude-based change point estimates during the PSI processing.

So far, the detection and analysis of TPS has primary been tested and evaluated in the context of construction activities (Ansari et al., 2014; Hu et al., 2019, 2024; Dörr et al., 2022a,c). These usually only feature a single change point in the case of new constructions over formerly uncultivated land.

2. Methods

In this section, we describe methods to identify and analyze ROPSs, which are used in this study. The section contains a recap of relevant TPS approaches from Dörr et al. (2022a), and provides the description of newly proposed detection and analysis approaches. The TPS phase unwrapping carried out during the analysis described in Section 4 followed the approach in Dörr et al. (2022a), which is why it is not described here.

2.1 Characteristics of Recurringly Occluded Persistent Scatterers (ROPSs)

We define ROPSs as PSs which are occluded in several segments of the InSAR time series. The occlusion may be caused, for example, by seasonal snow coverage or recurring flooding-induced water coverage. We assume that the coherent backscatter characteristics do not change during the occlusions, and that the incoherent backscatter characteristics of the occlusion periods also do not change significantly over time. Under these assumptions, ROPS backscatter can be described by a mixture probability distribution consisting of two probability density functions (pdfs). The marginal mixture pdf of the amplitude can then be assumed to be the weighted sum of the Rice (p_{rice}) and Rayleigh (p_{rayl}) distributions, which represent the PS and non-PS states, respectively:

$$p(A) = w p_{\text{rayl}}(A|\sigma_{\text{rayl}}) + (1-w) p_{\text{rice}}(A|\nu, \sigma_{\text{rice}}), \quad (1)$$

where w is a weight, σ_{rayl} and σ_{rice} are the scale parameters of the Rayleigh and Rice distributions, respectively, and ν the backscatter amplitude of the PS. The pdfs of the Rayleigh and Rice distributions are

$$p_{\text{rayl}}(A|\sigma_{\text{rayl}}) = \frac{A}{\sigma_{\text{rayl}}^2} \exp\left(-\frac{A^2}{2\sigma_{\text{rayl}}^2}\right), \quad (2)$$

$$p_{\text{rice}}(A|\nu, \sigma_{\text{rice}}) = \frac{A}{\sigma_{\text{rice}}^2} \exp\left(-\frac{A^2+\nu^2}{2\sigma_{\text{rice}}^2}\right) I_0\left(\frac{A\nu}{\sigma_{\text{rice}}^2}\right), \quad (3)$$

respectively, where I_0 denotes the modified Bessel function of first kind. We refer to the following ratios as to ROPS-SCR and ROPS-SNR, respectively: ROPS-SCR $= \nu/2\sigma_{\text{rice}}^2$, and ROPS-SNR $= \nu/2\sigma_{\text{rayl}}^2$.

The PSI analysis of such ROPSs requires that the periods are known in which the PSs are not occluded. The identification of these periods can be described as a change point detection problem. The interferometric information acquired during these periods can then be evaluated with standard PSI approaches to estimate displacement time series.

2.2 ROPS amplitude change point detection

The basis of the ROPSs detection is, as for other TPS types, the assumption that abrupt changes in the phase and coherence of a pixel correspond to abrupt changes in its amplitude (Ferretti et al., 2003). The amplitude of a ROPS is assumed to be significantly larger in its active periods compared to its occlusion periods. Based on this assumption, TPS candidates are usually detected as pixels which feature time series segments with significantly different backscatter amplitudes, since detecting changes in the amplitude is much more efficient than detecting coherence changes.

We here compare two amplitude change point detection algorithms. The first approach is the iterative F-Test proposed by Hu et al. (2019), which is also used in the approach by Dörr et al. (2022a). The aim of the test is to identify change points between amplitude time series segments which are characterized by significantly different Rayleigh scale parameters, whose unbiased estimator for an amplitude time series A_n with N independent observations is

$$\hat{\sigma}^2 = \frac{1}{2N} \sum_{n=1}^{N} A_n^2. \quad (4)$$

Even though the PS backscatter amplitude is usually described by means of a Rice distribution, it is assumed that the amplitudes of PS and non-PS states of TPSs are still characterized by significantly differing Rayleigh scale parameters. The approach successively tests each acquisition n as a potential change point with the following hypothesis test:

$$F = \frac{\hat{\sigma}_1^2}{\hat{\sigma}_2^2} \underset{H_0}{\overset{H_1}{\gtrless}} F_\alpha. \quad (5)$$

The null hypothesis H_0 states that the estimated Rayleigh scale parameters $\hat{\sigma}_1$ and $\hat{\sigma}_2$ of two time series segments, separated at acquisition n, are not significantly different. It is tested against the alternative hypothesis H_1 that they are significantly different. Under H_0, the ratio F of the scale parameters follows a central F-distribution with $2n$ and $2N-2n$ degrees of freedom. This characteristic is used to compute the threshold F_α under a significance level α, which has to be exceeded in order that H_0 is rejected. If the threshold is exceeded at more than one acquisition, the acquisition with the highest F-values is selected as a change point. Afterwards, the time series is separated at this acquisition, and each of the two resulting time series subsets are again searched for a change point. This procedure is recursively repeated until no further change points are identified.

We propose an alternative change point detection algorithm that bases on the CuSum algorithm by Torre et al. (2023), which adapts the idea of the CuSum change point detection to radar

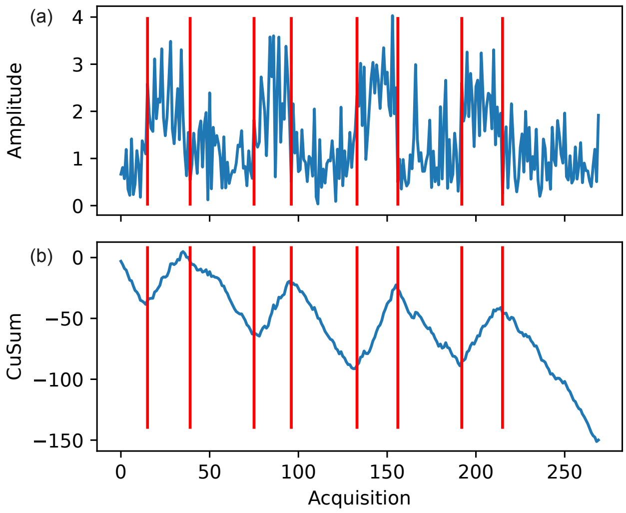

Figure 1. (a) Amplitude time series of a simulated ROPS with four PS segments, and five non-PS segments, separated by change points at the red lines. (b) CuSum measure S of the amplitude time series in (a), with distinct local extrema in the vicinity of the true amplitude change points.

data. The basic idea of the algorithm is to identify change points in radar amplitude time series by analyzing the cumulative sum of the instantaneous log-likelihood ratio (ILLR) s, which is the logarithmic ratio of the pdf values of the non-PS and PS states at acquisition n:

$$s(n) = \ln\left(\frac{p_{\text{rice}}(A(n)|\nu, \sigma_{\text{rice}})}{p_{\text{rayl}}(A(n)|\sigma_{\text{rayl}})}\right). \tag{6}$$

Torre et al. (2023) showed that the cumulative sum of s, denoted as S, features alternating minima and maxima at radar backscatter change points. Hence, multiple change points in a time series can be detected simultaneously by localizing significant extrema in the cumulative sum of s. The challenge is to suppress false alarms by defining a reasonable threshold for the extrema detection.

The parameters of the Rice and Rayleigh distributions have to be estimated prior to the ILLR computation. We here use the expectation-maximization (EM) algorithm to estimate the parameters of the mixture pdf in Equation 1 for each potential ROPS. The EM algorithm for the Rayleigh-Rice mixture parameter estimation is exemplarily described in Zanetti et al. (2015). The single iterations of the EM algorithm can be carried out simultaneously for all pixels of interest, enabling an efficient estimation. After the parameter estimation, the ILLR s (Equation 6) is computed and cumulatively summed up to get S. Instead of using the simulation-based approach by Torre et al. (2023) to define reasonable thresholds for the detection of significant extrema in S, we here use a simple prominence-based peak detection algorithm to find significant extrema in S in form of peaks in S and $-S$. The prominence threshold was empirically chosen as a multiple of the ratio $\hat{\nu}/\hat{\sigma}_{\text{rayl}}$.

The CuSum measure S is exemplarily displayed in Figure 1 for a simulated ROPS. It exhibits local minima and maxima in the vicinity of the amplitude change points. Differences in the location of the extrema and the true change points are caused by a low ROPS-SNR of 1.6.

2.3 ROPS segment selection

The ROPS segments, which have been segmented by the change point detection algorithm, are classified as PS or non-PS segments using an adaptive amplitude dispersion threshold. We apply the approach by Hu et al. (2024) to find the segment length depending threshold based on PS signal simulations.

2.4 ROPS parameter and coherence estimation

The TPS coherence estimation is described in Dörr et al. (2022a) and shortly recapped. The foundation of the parameter estimation is the model of a pixel's interferometric phase after the subtraction of the flat earth and topographic phase, which are simulated based on a given digital elevation model (DEM):

$$\phi = \phi_h + \phi_v + \phi_\alpha + \phi_{\text{nlin}} + \phi_{\text{tropo}} + \phi_{\text{sc}} + \phi_{\text{noise}}, \tag{7}$$

where ϕ_h, ϕ_v and ϕ_α are the phase contributions due to a local DEM error, a linear displacement rate, and a thermally induced displacement rate, respectively. ϕ_{nlin} is caused by nonlinear displacements, ϕ_{tropo} by tropospheric delays, and ϕ_{sc} comprises phase contributions with long spatial correlations lengths, such as ionospheric phase delays and phases due to tidally induced displacements. The goal of the (T)PS coherence estimation is to estimate and reduce phase contributions to get an estimate of the pixel's phase noise ϕ_{noise}, which determines whether the pixel is considered as a (T)PS or not.

The reduction of spatially correlated phase contributions of TPSs corresponds to that of PSs, thus is not described here. The displacement rate, height, and thermally induced displacement rate are estimated by the method of periodograms. This parameter estimation step is carried out with a fully connected multi-reference interferogram stack, contrary to the single-reference interferogram stacks usually used in the PSI. The size of the over-determined interferogram network allows us to build sub-band stacks, and a suitable choice of interferograms in these sub-band stacks enables to break the 3D parameter estimation problem into three 1D parameter estimation steps, which are carried out sequentially and iteratively. For example, the height error of TPSs candidates is estimated based on interferogram sub-stacks with a large perpendicular baseline bandwidth and small temporal and thermal baseline bandwidths. An advantage of using this estimation scheme is that it enables the treatment of pixels with different lifetimes, instead of the single-reference network estimation of standard PSI algorithms which excludes pixels whose coherent lifetime does not include the reference acquisition.

The integration of TPSs, including ROPSs, into the parameter estimation is achieved by introducing an interferogram weight w into the periodogram. The weight w is zero for interferograms outside and one for interferograms inside the PS periods of TPSs. The periodogram estimation is carried out using the truncated singular value decomposition (TSVD) of the design matrix that combines information on the parameter-specific interferogram baselines, and the parameters to be tested (Zhu and Bamler, 2010). We compare this approach with the compressive-sensing parameter estimation approach OCLeaS proposed in Rebmeister et al. (2021). The latter provides a computationally efficient hybrid tomography-PSI algorithm which combines the orthogonal matching pursuit and complex least squares. For the estimation of the OCLeaS objective function, the interferometric phase values are weighted the same way as in the periodograms.

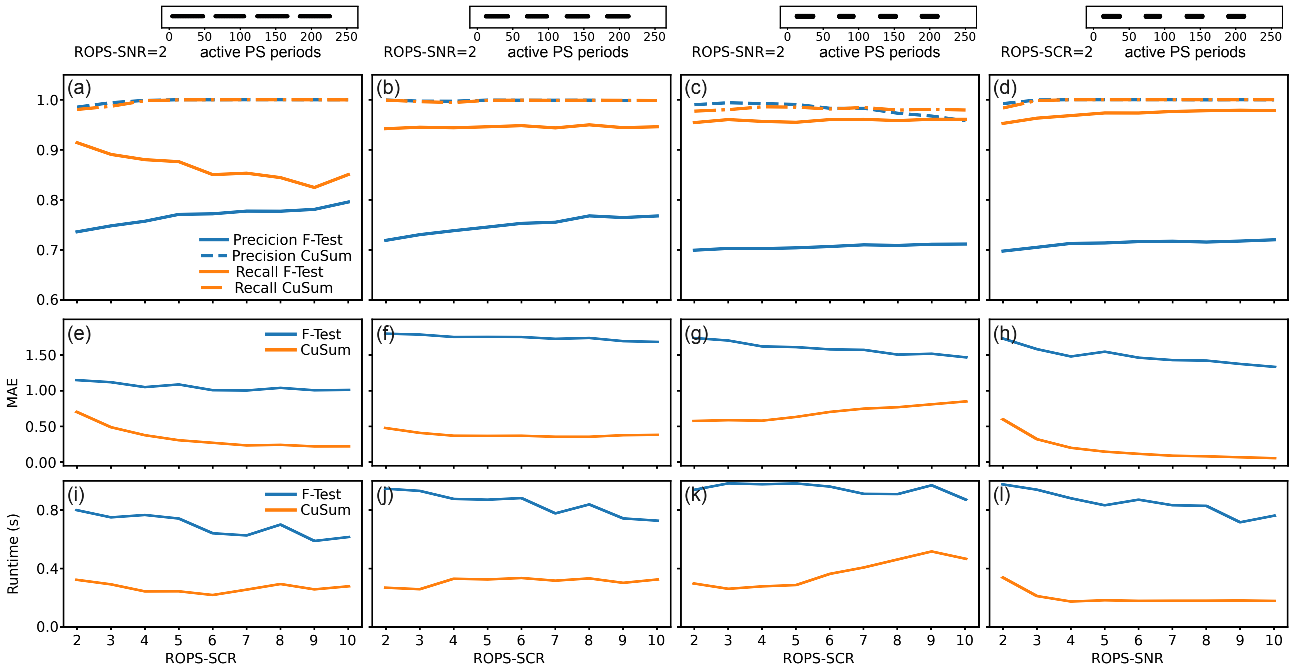

Figure 2. Comparison of change point detection performance metrics for the F-Test and CuSum approaches for different ROPS simulation scenarios. The columns show different metrics for the single simulation scenarios. The active PS periods within the simulated time series of 270 scenes are visualized on top of the columns in form of black bars. The ROPS-SNR is fixed to 2 in columns 1-3, whereas the ROPS-SCR is fixed to 2 in column 4. (a)-(d) Precision and recall for both detection approaches, (e)-(h) the mean absolute error (MAE) of true positive change point detections, (i)-(l) the detection runtime.

3. Simulation Results

In this section, experimental results for the change point detection and parameter estimation are described for simulated ROPSs. The simulations were carried out for different occlusion and PS period lengths, as well as different ROPS-SCR and ROPS-SNR values.

3.1 Change point detection

We simulated ROPSs time series with 275 acquisitions, which corresponds to a period of approximately 4.5 years for a satellite revisit time of six days, as in the case of Sentinel-1. The simulated ROPSs feature two change points per year and varying ratios of PS to occlusion period lengths. With these settings, ROPSs with varying ROPS-SCR and fixed ROPS-SNR were simulated, as well as ROPSs with fixed ROPS-SCR and varying ROPS-SNR. We simulated 1,000 ROPSs for each scenario.

Precision and recall metrics for the F-Test- and CuSum-based change point detections for the simulated ROPSs amplitude time series are displayed in Figure 2. A detected change point was classified as true positive, if it was less than eight samples distant from a simulated change point. The figure also displays the MAE of true positives, and the runtime of the detection.

Overall, the CuSum approach shows a better and faster performance under all tested scenarios. Precision and recall of the CuSum are close to 1.0 in all scenarios, while these are largely different for the F-Test procedure. We tested different significance levels for the F-Test to derive more consistent precision and recall metrics, but no other tested significance level yielded better overall metrics. In general, the F-Test precision is lower than 0.8, indicating a significant amount of false positive detections. At the same time, the recall of the F-Test is less than 1.0 in all scenarios, which means that not all change points have been identified. The best performance with the F-Test was achieved for ROPSs with similarly long PS and occlusion periods, which was expected since the test generally struggles to identify short segments.

The MAE of true positive change points and the detection runtime are considerably better for the CuSum than for the F-Test in all scenarios. Interestingly, both metrics increase with increasing ROPS-SCR in the third simulation scenario (Figures 2 (g,k)). As the runtime for the CuSum algorithm is strongly dependent on the runtime of the iterative EM parameter estimation of the Rayleigh-Rice mixture distribution, we assume that the algorithm had problems to estimate the distribution parameters in that scenario. This also manifested in form of a slight precision decrease with increasing ROPS-SCR.

3.2 Parameter estimation

We simulated five years of phase time series for 1000 ROPSs, based on real baseline settings of the Sentinel-1 stack used in Section 4, which was acquired with a six day revisit cycle between 2017 and 2021. The simulated ROPSs feature two change points per year, with occlusion periods over the winters. The ratios of PS to occlusion period lengths varied for the different simulation scenarios, while the ROPS-SCR and ROPS-SNR values were fixed to two. The simulated ROPSs had a height error of 10 m and a displacement rate of 0 mm/yr. We neglected a thermally induced displacement rate in this simulation, but simulated a seasonally undulating displacement with a frequency of 1/yr and an amplitude of 3 mm in half of the scenarios. We simulated 1,000 ROPSs for each scenario.

The averaged objective functions of the estimation of the linear displacement rate, normalized by their maximum values,

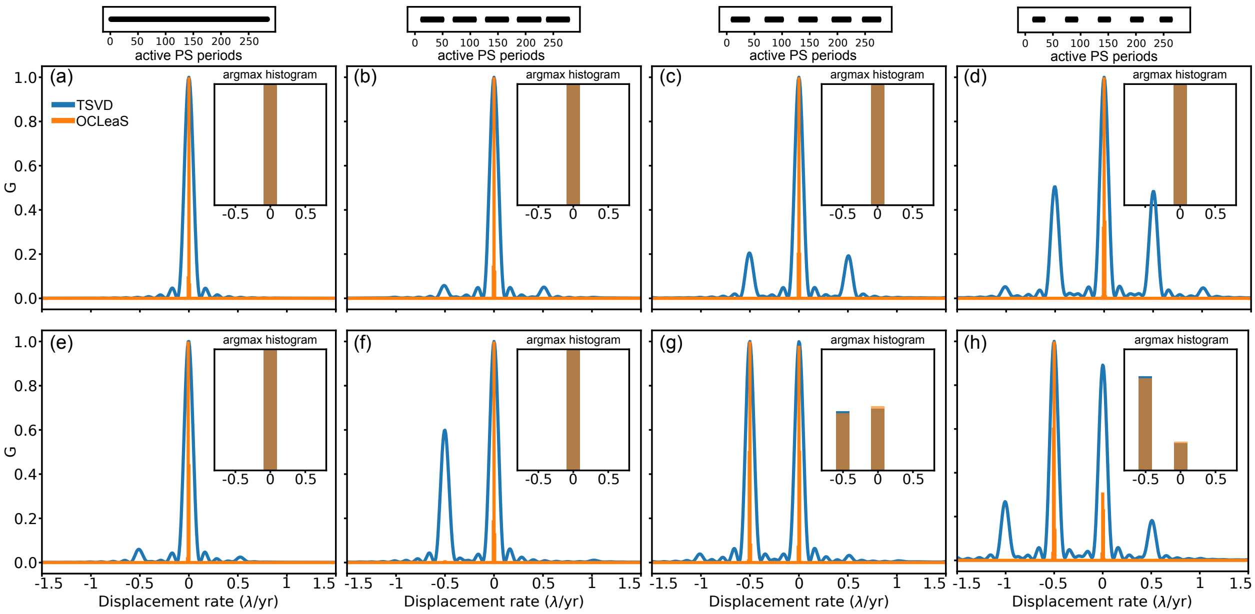

Figure 3. Averaged stacked objective functions of the displacement rate estimation for different simulation scenarios with 1000 ROPS each. The coherent periods within the five years time series are visualized on top of the columns in form of black bars. The ROPS-SCR and ROPS-SNR values were consistently fixed to two. All ROPSs were simulated with a displacement rate of 0 mm/yr. Seasonal displacements with a frequency of 1/yr and an amplitude of 0 mm and 3 mm were simulated in (a)-(d) and (e)-(h), respectively.

for all the scenarios and the TSVD and OCLeaS estimation methods are displayed in Figure 3. In addition to the averaged objective functions, the Figure also displays histograms of the maximum locations in the objective functions of the simulated ROPSs. The parameter estimation results show that the simulated displacement rate of 0 mm/yr is correctly estimated for all scenarios without seasonal displacements, but in the TSVD results, secondary peaks at multiples of 0.5 λ/yr are becoming stronger with a decreasing PS to occlusion time ratio per observation year. The reason behind is an increasingly inadequate time series sampling. The shorter the observation time per year, the better displacement rate multiples of 0.5 λ/yr (corresponding to a phase of a multiple of 2π during one year) could explain the observations. If the simulated displacement rate is nonzero, the objective functions simply shifts along the x-axis.

In the case of ROPSs with seasonally undulating displacements with an amplitude of 3 mm, the objective functions feature even stronger secondary peaks at multiples of 0.5 λ/yr. From a PS to occlusion period ratio of approximately 0.5, the maxima of the objective functions from the TSVD and OCLeaS increasingly do not reflect the true simulated displacement rate. The reason behind is two-fold: The previously described sampling problem is accompanied by an incomplete sampling of the seasonally undulating displacement, which, under unfavorable relation between undulation phase and sampling window, is implicitly interpreted as linear motion. The performance of the TSVD and the OCLeaS estimation approaches is very similar in all scenarios. However, the significance of the estimation can be better assessed for the TSVD periodograms, which is why we stuck with this method in the Sentinel-1 experiment described in Section 4. The maxima in Figure 3 (g,h) were marked as insignificant single peaks by the applied significance test, which is a combination of the Fisher g-test and an assessment of the magnitude ratio of the two strongest peaks. We observed that the described estimation instability got worse for increasing seasonal signal amplitudes.

4. Sentinel-1 Experiment

We tested the PSI approach with the newly proposed CuSum change point detection and the TSVD-based parameter estimation with a Sentinel-1 dataset acquired over a high-alpine region in the Oetztal Alps, which is affected by long periods of snow-cover during the year. The data and the results are described and discussed in the following.

4.1 Data

We used 285 VV-polarized Sentinel-1 scenes, which were acquired in the interferometric wide swath mode between January 2017 and December 2021 over the Oetztal Alps in Austria in the descending orbit (Figure 4). The time period was selected like this to have a time series with a continuous revisit time of 6 days, before Sentinel-1B failed in late December 2021. The interferometric pre-processing was carried out with the software ISCE (Rosen et al., 2012), using the Copernicus digital elevation model with a spatial resolution of 30 m. The reference scene was acquired on July 11, 2019.

4.2 Results and discussion

Identified change points. The histograms of the number of identified change points per PS and ROPS before and after the amplitude dispersion based segment selection (Section 2.3) are displayed in Figure 4 (a). They show that the most common change point counts before and after the segment selection were nine and four, respectively, revealing that the segment selection step in the algorithm led to a significant reduction of change points by merging apparently incoherent consecutive segments. Figure 4 (c) shows the counts of identified change point dates before and after the segment selection. It features nine distinct peaks around May/June and October/November of each year, aligning with typical snow melt and first snow fall periods in this region, respectively. In the last year, the October/November

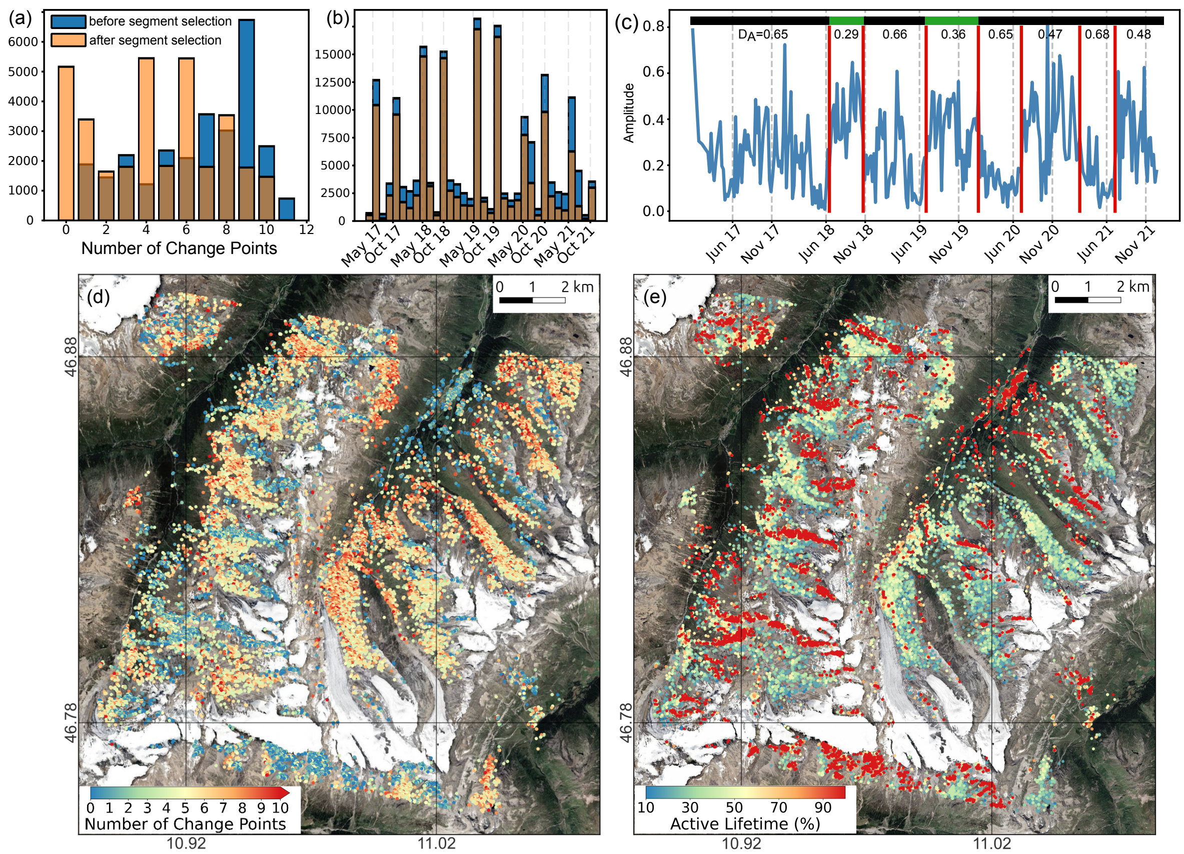

Figure 4. (a)-(b) Histograms of change point counts and change dates of identified (RO)PS before and after the segment selection step (Section 2.3). (c) Amplitude time series of a ROPS with original change points indicated in red, and accepted and rejected PS segments in green and black, respectively. (d)-(e) Change point count and active Lifetime of (RO)PS, respectively. The latter is the ratio of the number of coherent acquisitions to the total number of acquisitions in the time series. Imagery: Google Earth, ©2026 Airbus.

peak is not as pronounced, probably because the segment afterwards is quite short, hence difficult to be detected by the change point detection algorithm. The figure also reveals that the change points in the last two years were especially removed by the segment selection step. An example amplitude time series with detected change points and selected PS segments is displayed in Figure 4 (c). Seven change points were detected at this points, but only four change points were kept after the segment selection. We assume that the last segment has been removed for lots of pixels as the last winter onset could not be detected robustly, increasing the noise in that segment.

The location of all identified measurement points is displayed in Figure 4 (d) and (e). The points are color-coded by their count of identified change points in (d) and by their active lifetime in (e), which is the ratio of the number of coherent acquisitions to the total number of acquisitions in the time series. Both measures show a spatial correlation, which indicates that the change point detection algorithm yields consistent results for points with similar backscatter changes over time. The active lifetime of ROPSs also correlates with the number of change points. PSs without any change points were mainly found on steep south-facing slopes, where probably little snow accumulates in general, as well as in the lower parts of the study area, including the village of Obergurgl. TPSs with one single change point were mainly identified at locations where also PSs were found, indicating that these are probably points whose temporal coherence change was not affected by seasonal snow cover, but by other causes such as construction activity in Obergurgl. For other TPSs, there is a tendency of a decreasing count of identified change points with increasing elevation. ROPS with less than nine change points are mainly located at locations where the EGMS results for the time series between 2018-2022, which excluded presumably snow-covered scenes, did not feature any PSs (Figure 5). This indicates that some summer acquisition were probably affected by noise at the affected pixels, e.g. by temporary snow cover, which led to a coherence decrease and rejection of the affected pixels in the EGMS. On the contrary, the specific summer segments were removed in our approach by the segment selection step. However, we assume that also these summers featured acquisitions with PS backscatter characteristics at the affected pixels, and it would be desirable in the future to incorporate all usable ROPS acquisitions into the PSI analysis. This would require to move away from the assumption of coherent segments to the classification of coherent/incoherent acquisitions.

Displacement estimates. The estimated LOS displacement rates of identified PSs and ROPSs are compared to the EGMS level 2A results for the time series between 2018-2022 in Figure 5. The used colormap marks estimated displacement rates of -25.5 to -31 mm/yr and 25.5 to 31 mm/yr in pink, as these rates are distributed around the $\pm 0.5\ \lambda$/yr, which were found to be potential false estimations for ROPSs in Section 3.2. The figures show that the EGMS features considerably more points with displacement rates in those range compared to our results, which indicates that our approach might be more capable of identifying and rejection such false estimations. However, it is

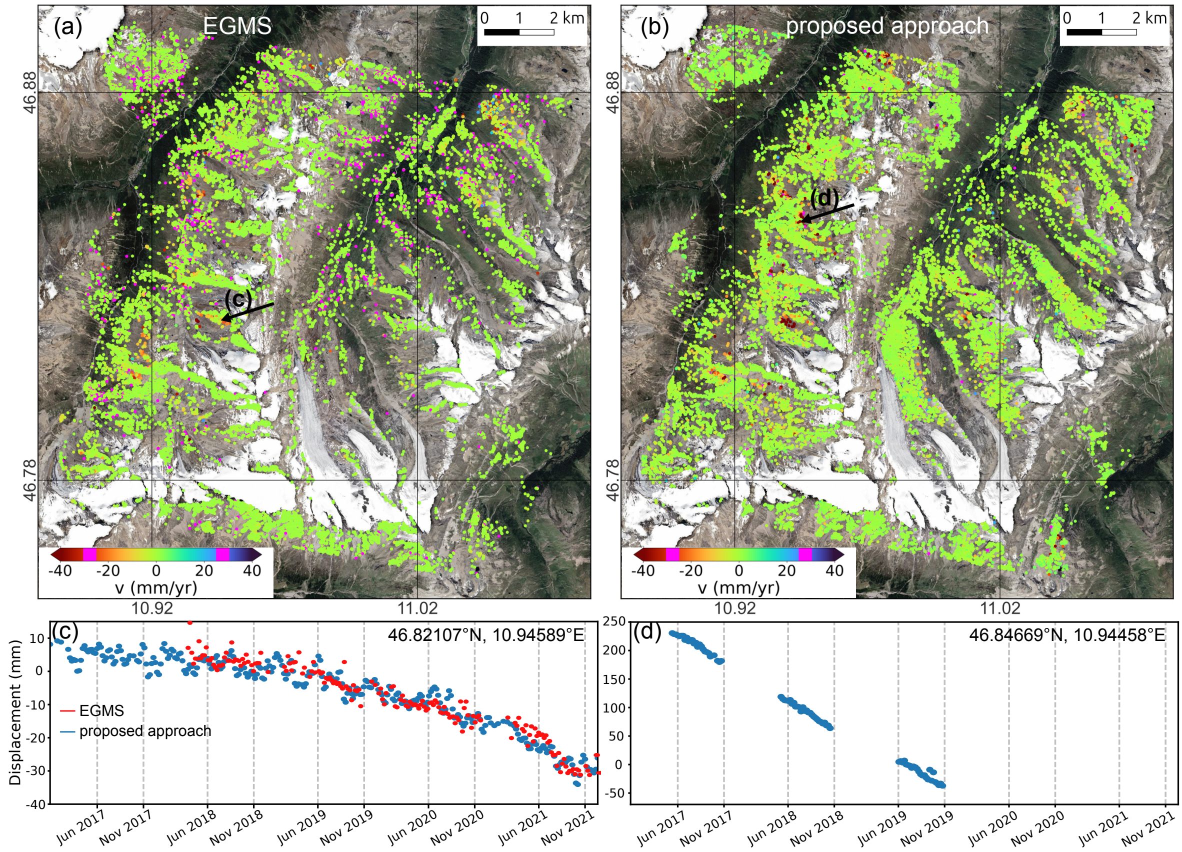

Figure 5. (a)-(b) Estimated line-of-sight (LOS) displacement rates from the EGMS 2018-2022 results and our approach, respectively. (c)-(d) Exemplary averaged displacement time series of pixels in a radius of 50 m around the given coordinates. The locations are also indicated by arrows in (a) and (b). Imagery: Google Earth, ©2026 Airbus.

challenging to evaluate this in a proper way, as (i) pixels might have actual displacement rates in those value range, and (ii) further false estimations could be outside of the marked value ranges, since the periodogram peaks around $\pm 0.5\ \lambda$/yr in Figure 3 shift along the x-axis for non-zero true displacement rates. This means that a pixel could have a falsely estimated displacement rate of $0.8\ \lambda$/yr if its actual displacement rate is $0.3\ \lambda$/yr, for example.

Apart from the points marked in pink, the results from EGMS and our approach show similar displacement rates in areas where both methods identified measurement pixels. As an example, both results show some faster moving areas on the western mountain ridge, which might be rock glaciers or instable slopes. An exemplary comparison of averaged time series of measurement pixels in a 50 m radius around a location on such a slope is displayed in Figure 5 (c). The overlapping displacement time series of EGMS and our approach are very similar at this location, with an increasing displacement rate over time. The noise level in our result is slightly higher, which might be related to differences in the post-processing.

The spatial density of the measurement points differs significantly between both results in certain areas. Our approach identified more points in many highly elevated areas, such as east of the Gurgler Ferner glacier. It also identified more fast moving pixels on the western mountain ridge, with estimated displacement rates of up to -140 mm/yr. An example time series of such a fast moving location is displayed in Figure 5 (d), where ROPS with three coherent, consecutive summer segments have been identified, whose estimated displacement was about -270 mm in the progress of the three summers. It would be helpful to validate these results with measurements from other geodetic sources in the future, such as photogrammetric measurements. Finally, there are also some areas where the measurement pixel density was lower in our results compared to the EGMS, which is caused by fundamental differences in the PSI processing. Our approach uses a spatial averaging approach to eliminate long-wave phase contribution from the observations (Equation 7), which can lead to problems in some areas with high topographic gradients. The approach used by the EGMS is based on a phase triangulation network, which reduces such topographic-related challenges. On the other hand, the phase averaging in spatial patches allows for more straight-forward TPS integration, and we aim at improving this approach for areas with large topographic gradients in the future.

5. Discussion and Conclusions

We here presented a first evaluation of the capabilities of the TPS integrating PSI approach from Dörr et al. (2022a) to identify and analyze ROPSs. We showed that a newly proposed CuSum change point detection algorithm outperforms the F-Test approach implemented in the tested PSI algorithm, and can robustly identify the coherent time series segments of simulated ROPSs. Additionally, we showed that the estimation of the displacement rate of ROPSs becomes more instable with increasing occlusion period lengths, increasing the probability of an overestimation. For this reason, it is important that the satellite revisit time is as short as possible, so that there are as many observations as possible in the coherent lifetime segments. Moreover, seasonal movements which are inadequately sampled during short coherent ROPS segments can also lead to considerably false displacement rate estimations. However, the characteristics of the estimation periodograms can be used to mark such points as unreliable.

Applied to Sentinel-1 data acquired over the Oetztal Alps, which are affected by long periods of snow cover during the year, the algorithm was able to identify many ROPSs with differing active lifetimes. For most of the identified ROPSs, coherent lifetimes were identified during summers, as expected, but not each summer of the observation time was identified as coherent for most of the points. The reason behind was probably temporary phase noise in the affected summers due to temporary snow cover or vegetation, or fuzzy transition phases between the non-PS and PS states. We still assume that such summers contained usable acquisitions in many cases. This highlights a disadvantage of the approach, which assumes that ROPSs have coherent time series segments of a certain length. It would be desirable to move away from this assumption in the future to a system which manages to classify all SAR acquisitions of a pixel into ”usable for PS analysis” or ”not usable”. Still, our approach provided a significant better spatial measurement point coverage in the study area compared to EGMS, and moving areas such as unstable slopes or rockfalls could be identified, even if just observation from two out of five summer months were used for the analysis. Lastly, we showed that the EGMS featured significant more potential false displacement rate estimations than our approach, which indicates that our approach is able to better identify and reject affected pixels.

References

Ansari, H., Adam, N., Brcic, R., 2014. Amplitude time series analysis in detection of persistent and temporal coherent scatterers. *2014 IEEE Geoscience and Remote Sensing Symposium*, IEEE, Quebec City, QC, 2213–2216.

Dogan, O., Perissin, D., 2014. Detection of Multitransition Abrupt Changes in Multitemporal SAR Images. *IEEE Journal of Selected Topics in Applied Earth Observations and Remote Sensing*, 7(8), 3239–3247. https://ieeexplore.ieee.org/document/6704799/.

Dörr, N., Schenk, A., Hinz, S., 2022a. Fully Integrated Temporary Persistent Scatterer Interferometry. *IEEE Transactions on Geoscience and Remote Sensing*, 60, 1–15. https://ieeexplore.ieee.org/document/9862970/.

Dörr, N., Schenk, A., Hinz, S., 2022b. On the Relevance of Temporary Persistent Scatterers for Long-Term PS-InSAR Monitoring. *EUSAR 2022; 14th European Conference on Synthetic Aperture Radar*, 1–6.

Dörr, N., Schenk, A., Hinz, S., 2022c. Systematic Analysis of Initial Settlement of new Constructions in the Mekong Delta by Coherence Change Detection of Temporary Persistent Scatterers. *IGARSS 2022 - 2022 IEEE International Geoscience and Remote Sensing Symposium*, IEEE, Kuala Lumpur, Malaysia, 1111–1114.

Ferretti, A., Colesanti, C., Perissin, D., Prati, C., Rocca, F., 2003. Evaluating the effect of the observation time on the distribution of sar permanent scatterers. *Proc. of FRINGE 2003 Workshop, Frascati, Italy*.

Ferretti, A., Prati, C., Rocca, F., 2001. Permanent scatterers in SAR interferometry. *IEEE Transactions on Geoscience and Remote Sensing*, 39(1), 8–20. https://ieeexplore.ieee.org/document/898661.

Ferretti, A., Savio, G., Barzaghi, R., Borghi, A., Musazzi, S., Novali, F., Prati, C., Rocca, F., 2007. Submillimeter Accuracy of InSAR Time Series: Experimental Validation. *IEEE Transactions on Geoscience and Remote Sensing*, 45(5), 1142–1153. http://ieeexplore.ieee.org/document/4156314/.

Hooper, A., Segall, P., Zebker, H., 2007. Persistent scatterer interferometric synthetic aperture radar for crustal deformation analysis, with application to Volcán Alcedo, Galápagos. *Journal of Geophysical Research: Solid Earth*, 112(B7), 2006JB004763. https://agupubs.onlinelibrary.wiley.com/doi/10.1029/2006JB004763.

Hu, F., Gong, Y., Cheng, S., Xu, F., 2024. Amplitude-Aided 3-D Phase Unwrapping for Temporary Coherent Scatterers Interferometry. *IEEE Transactions on Geoscience and Remote Sensing*, 62, 1–15. https://ieeexplore.ieee.org/document/10596312/.

Hu, F., Wu, J., Chang, L., Hanssen, R. F., 2019. Incorporating Temporary Coherent Scatterers in Multi-Temporal InSAR Using Adaptive Temporal Subsets. *IEEE Transactions on Geoscience and Remote Sensing*, 57(10), 7658–7670. https://ieeexplore.ieee.org/document/8756305/.

Perissin, D., Ferretti, A., 2007. Urban-Target Recognition by Means of Repeated Spaceborne SAR Images. *IEEE Transactions on Geoscience and Remote Sensing*, 45(12), 4043–4058. https://ieeexplore.ieee.org/document/4378562.

Rebmeister, M., Schenk, A., Bradley, P. E., Dörr, N., Hinz, S., 2021. OCLeaS – A tomographic PSI Algorithm using Orthogonal Matching Pursuit and Complex Least Squares. *Procedia Computer Science*, 181, 220–230. https://linkinghub.elsevier.com/retrieve/pii/S1877050921001836.

Rosen, P. A., Gurrola, E., Sacco, G. F., Zebker, H., 2012. The InSAR scientific computing environment. *EUSAR 2012; 9th European Conference on Synthetic Aperture Radar*, 730–733.

Torre, A., Taylor, A., Poullin, D., Chonavel, T., 2023. Parameters Extraction of Unknown Radar Signals Using Change Point Detection. *2023 IEEE International Radar Conference (RADAR)*, 1–6.

Zanetti, M., Bovolo, F., Bruzzone, L., 2015. Rayleigh-Rice Mixture Parameter Estimation via EM Algorithm for Change Detection in Multispectral Images. *IEEE Transactions on Image Processing*, 24(12), 5004–5016. http://ieeexplore.ieee.org/document/7229300/.

Zhu, X. X., Bamler, R., 2010. Very High Resolution Spaceborne SAR Tomography in Urban Environment. *IEEE Transactions on Geoscience and Remote Sensing*, 48(12), 4296–4308. http://ieeexplore.ieee.org/document/5497277/.